arXiv:0902.3457v1 [astro-ph.EP] 19 Feb 2009

KUIPER BELT OBJECT OCCULTATIONS: EXPECTED RATES, FALSE POSITIVES, AND SURVEY DESIGN

S.J. Bickerton
Department of Astrophysical Sciences, Princeton University, Princeton, NJ 08544

D.L. Welch
Department of Physics & Astronomy, McMaster University, Hamilton, ON L8S 4M1

and

JJ. Kavelaars
Herzberg Institute of Astrophysics, Victoria, BC V9E 2E7
Draft version February 19, 2009

ABSTRACT

A novel method of generating artificial scintillation noise is developed and used to evaluate occultation rates and false positive rates for surveys probing the Kuiper Belt with the method of serendipitous stellar occultations. A thorough examination of survey design shows that: (1) diffraction-dominated occultations are critically (Nyquist) sampled at a rate of 2 Fsu^{-1}, corresponding to 40 s^{-1} for objects at 40 AU, (2) occultation detection rates are maximized when targets are observed at solar opposition, (3) Main Belt Asteroids will produce occultations lightcurves identical to those of Kuiper Belt Objects if target stars are observed at solar elongations of: $116° \lesssim \varepsilon \lesssim 125°$, or $131° \lesssim \varepsilon \lesssim 141°$, and (4) genuine KBO occultations are likely to be so rare that a detection threshold of $\gtrsim 7 - 8\sigma$ should be adopted to ensure that viable candidate events can be disentangled from false positives.
Subject headings: atmospheric effects, occultations, Kuiper Belt, Solar System: formation

1. INTRODUCTION

A method of detecting km-sized Kuiper Belt Objects (KBOs) is that of serendipitous stellar occultations (SSO). Km-sized KBOs are too faint to be observed directly, but can, in theory, be detected indirectly. The passage of a KBO through the line of sight to a background star will produce a characteristic perturbation in the observed stellar photometric time series, serendipitously revealing the presence of the occulter. The method was originally proposed by Bailey (1976), and has been developed extensively (Dyson 1992; Brown & Webster 1997; Roques & Moncuquet 2000; Cooray 2003; Cooray & Farmer 2003; Gaudi 2004; Nihei et al. 2007). Both optical (Roques et al. 2004, 2006; Zhang et al. 2008; Bickerton et al. 2008, hereafter BKW), and x-ray (Chang et al. 2006; Jones et al. 2006) occultation searches have been used to probe the population of the trans-Neptunian region. In this paper, we evaluate a variety of issues which are central to planning, and performing a KBO occultation survey. The methods we've used in our analyses are presented in Section 2, and results for the issues examined are presented in Section 3.

Much of the work presented herein is based on the planting and recovery of occultation profiles in synthetic photometric time series. Great care must be taken to reproduce the atmospheric scintillation properties of real photometric data, and we begin in Section 2.2 by developing a method of generating artificial time series to reproduce the properties of real time series in both the time domain and the frequency domain.

The SSO method was examined in the context of the Kuiper Belt (Roques & Moncuquet 2000, hereafter R&M) before a break in the KBO size distribution had been identified (Bernstein et al. 2004) or confirmed (Fuentes & Holman 2008; Fraser & Kavelaars 2009). In Section 3.1, we present updated KBO occultation rate estimates based on a broken power-law size distribution for the KBOs, and with consideration for the detectability of diffraction-dominated occultation events.

Photometric time series in KBO occultation surveys have been obtained at a variety of sampling frequencies: 5 s^{-1} (Zhang et al. 2008), 40 s^{-1} (BKW), and 45 s^{-1} (Roques et al. 2006). In Section 3.2, we show how Fourier methods can be used to establish a critical (Nyquist) sampling rate for occultation work. Numerical tests of the theory are presented in Section 3.4.

The probability an occultation will occur is proportional to the perpendicular-projected velocity of the occulter with respect to the Earth. For the Kuiper Belt, the motion is retrograde and the velocity is maximized by conducting observations at solar opposition (R&M). In Section 3.3, we consider the possibility that off-opposition observations could improve the detectability of smaller, and potentially more numerous objects.

It is often useful to know the diameter of the smallest detectable object for data with a given signal to noise. In Section 3.5, we show how the signal to noise ratio, hereafter S/N, determines the minimum detectable size.

Interest in small body occultations has focused largely on the Kuiper Belt, but other near-field objects are capable of producing occultations. The size/distance degeneracy for occultation events has been assessed by Cooray (2003), with a discussion on how it may be broken for diffraction-dominated events. In Section 3.6, we evaluate the size/distance degeneracy further to determine the size/distance an occulter must have to produce an event

Electronic address: bick@astro.princeton.edu
Electronic address: welch@physics.mcmaster.ca
Electronic address: JJ.Kavelaars@nrc-cnrc.gc.ca

identical to a KBO occultation. We then consider the possibility of degeneracy with the Main Belt Asteroids (MBAs).

We close in Section 3.7 with an evaluation of how atmospheric scintillation influences the false positive occultation rate. We then compare false positive rates to the expected rates for real occultations to determine an appropriate detection threshold.

Results are discussed and summarized in Sections 4, and 5, respectively.

2. METHODS OF ANALYSIS

Optimization of the observing parameters in occultation work requires a metric by which the different parameters can be compared. We have chosen to measure how successfully an event can be detected with a 'plant and recover' strategy. There are three contributing components in this approach: a simulated occultation lightcurve, a simulated photometric time series, and a detection algorithm.

2.1. *Simulating Occultation Lightcurves*

Diffraction effects become significant in an occultation when the occulting object has a radius smaller than the Fresnel scale unit, 1 Fsu $= (\lambda d/2)^{1/2}$, where λ is the wavelength of observation, and d is the distance to the occulter. At 40 AU the Fresnel scale for 550 nm light is 1285 m. A successful occultation lightcurve model for a km-sized KBO must therefore take into account diffraction effects (Roques et al. 1987; Nihei et al. 2007; Bickerton et al. 2008). We have adopted a lightcurve modeling method described by Roques et al. (1987) in which a circular occulting mask is assembled by placing progressively smaller rectangles at the periphery of the mask. Five "orders" of these rectangles have been used for all occultation lightcurve models in this work.

All models were numerically integrated over a stellar disk with a projected size appropriate for the distance to, and spectral type of, the star being considered. Similarly, models were numerically integrated over a 400-700 nm passband.

2.2. *Simulating Photometric Time Series*

The evaluation of false positive rates (Section 3.7) requires that realistic artificial time series be analyzed. Dravins et al. (1997) showed that scintillation in a photometric time series produces a power spectrum which decreases as a function of frequency. An artificial power spectrum can be generated and tailored to reproduce the properties of an observed one, and this artificial power spectrum can then be inverse-Fourier transformed to produce a time series which has the same statistical properties – both in time and frequency – as the original 'real' data set.

2.2.1. *The Power Spectra of Photometric Time Series*

Discrete Fourier transforms (see, for example Bracewell 1986) of the photometric time series described in BKW were computed with a fast Fourier transform (FFT) algorithm. FFT algorithms are most efficient for time series composed of $N = 2^n$ points, where n is an integer, and the time series were truncated to have the largest number of points which satisfied this requirement. The real and

imaginary frequency components for a 409.5 s time series (2^{14}=16384 points at 40 s^{-1}) are shown in the upper panels of Figure 1. The amplitude of the components decreases as a function of frequency. Each frequency component was normalized by the standard deviation of the values within ± 0.5s^{-1}, and the normalized frequency component distributions are presented in the lower panels of Figure 1. The frequency components are consistent with Gaussian variates at 95% confidence (based on reduced χ^2 tests).
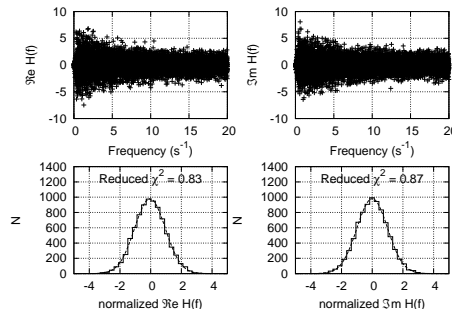

FIG. 1.— The noise distributions of the real and imaginary parts of $F(\omega)$. Upper panels show the real (left) and imaginary (right) frequency components. The frequency components were normalized by the standard deviation of points within ± 0.5s^{-1}, and are shown as histograms in the lower left (real) and right (imaginary) panels with best-fit Gaussians. The frequency components are consistent with Gaussian variates based on reduced χ^2 values.

The power spectrum corresponding to Figure 1 is shown in Figure 2 and can be seen to obey $\log |F|^2 \propto \beta \log f$, or $|F|^2 \propto f^\beta$, where $|F|$ is the norm of the frequency components, f is the frequency, and β is the power law slope. The power spectrum approaches a value of zero as the highest frequency is approached, indicating that aliasing effects are likely to have been minimized (Press et al. 1992). In observed photometric time series, no relationship between phase and frequency was expected or observed.
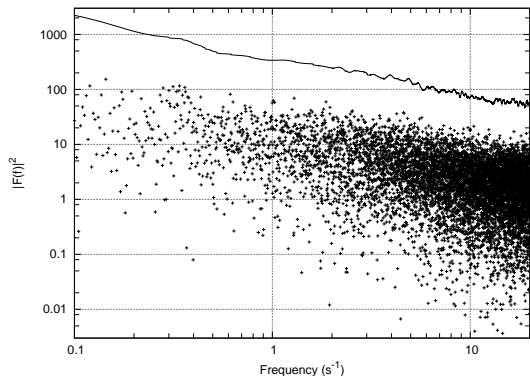

FIG. 2.— The power spectrum for a 40 s^{-1} photometric time series showing a power law relationship of $|F| \propto f^\beta$, with $\beta \approx 1$. The trend of the average power (0.2 s^{-1} bins) is shown offset above for clarity.

The photometric time series reported in BKW (56 separate 7-25 minute segments) were Fourier transformed

to produce power spectra and the power law slopes were measured with linear least squares for frequencies: $0.1 \text{ s}^{-1} < f < 20 \text{ s}^{-1}$. The measured slopes were normally distributed with $\overline{\beta} = -1.0$, and $\sigma_\beta = 0.3$. The value of β was not observed to vary as a function of frequency. As the time series were found to contain no detectable occultation events, the structure in these power spectra reflects the properties of the noise.

2.2.2. *Generating Artificial Time Series*

Generation of artificial time series began with the generation of artificial frequency components $\Re H(f_n)$ and $\Im H(f_n)$. The frequency components were inverse Fourier transformed to generate the time series.

$$h_k = \frac{1}{N} \sum_{n=0}^{N-1} H_n e^{-2\pi i k n/N}. \tag{1}$$

At a frequency, f_n, the real and imaginary components were assigned with phases, θ_n, amplitudes, a_n, and a normalizing constant, A, to produce a power spectrum with slope β:

$$\Re \ H(f_n) = f_n^{\beta/2} A \ a_n \cos(\theta_n), \quad \text{and} \tag{2}$$

$$\Im \ H(f_n) = f_n^{\beta/2} A \ a_n \sin(\theta_n). \tag{3}$$

The phase angles were drawn from a uniform random distribution with $-\pi \le \theta < \pi$, and the amplitudes, a_n, were drawn from a Gaussian distribution with $\overline{a}=0$, and $\sigma_a = 1$.

To produce a time series which is entirely real-valued, the property of conjugate symmetry (see, for example Bracewell 1986) requires that the spectral components for the negative frequencies are the complex conjugates of their positive counterparts, $F(f_{N-n}) = F^\star(f_n)$.

From the definition of the Fourier transform, $H(0)$ is determined by the mean, $\overline{h}$, of the time series being produced:

$$H_k = \sum_{n=0}^{N-1} h_n \ e^{2\pi i k n/N}, \tag{4}$$

$$H_0 = \sum_{n=0}^{N-1} h_n = N\overline{h}, \tag{5}$$

where N is the number of points.

The normalization constant, A, was chosen to produce the desired noise level, σ_h, in the time series (see Appendix A):

$$A = N\sigma_h \left[\sum_{n=0}^{N-1} f_n^\beta a_n^2 \right]^{-1/2}. \tag{6}$$

Frequency and time components for a 128-point artificial data set are presented in Figure 3 to illustrate the method[1].

The variates of a true photometric time series are log-normally distributed; but for variances of $(\sigma_h/\overline{h})^2 \lesssim 0.1$,

---

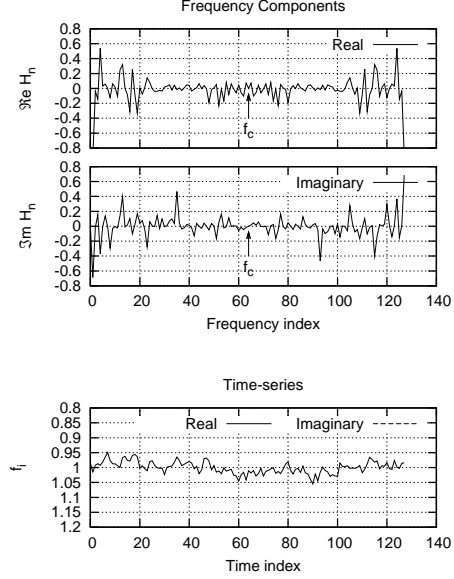[1] The code used to compute the algorithm is freely available from SJB.

FIG. 3.— Artificially-generated real (top) and imaginary (middle) frequency components, and the corresponding time series (bottom). A complex time series is produced, but the imaginary components all have values of zero due to conjugate symmetry.

the distribution is indistinguishable from a Gaussian (Dravins et al. 1997). If the chosen noise level (σ_h) is too high, the method will produce some negative variates, inconsistent with photometric measurements. This method should only be considered valid for noise levels of a few percent, $\sigma_h/\overline{h} \lesssim 0.1$.

One notable difference between observed and artificial photometric time series is the variability in the noise level. Atmospheric transparency can change on time scales of a few minutes during an observation, and airmass changes can be present in longer observations. The associated changes in the flux level can be normalized by smoothing, but normalization of the noise level (eg. by a moving standard deviation) would distort the amplitude of an occultation signal. To model a time series containing significant changes in the overall photometric noise level, the method above can be extended by modulating the amplitude of the artificial time series.

If photometric noise levels are below a few percent, and remain stable throughout a time series, an artificial time series data can be generated to simulate scintillation effects consistent with the real photometric measurements. The artificial time series will have the same statistical properties as the real data in both the time domain, and the frequency domain.

2.3. *The Detection Algorithm*

There are three different detection methods used to identify occultation events in photometric time series: the variability index (Roques et al. 2006), the cross-correlation of template lightcurves (Bickerton et al. 2008), and the rank probability method (Zhang et al. 2008). The cross-correlation of template occultation lightcurves has been used in this work.

Artificial time series, t_i, were generated for a given sampling rate (Section 2.2), and template occultation lightcurves were constructed (Section 2.1). The occul-

tation lightcurves were discretely sampled at the same rate as the time series to form cross-correlation test kernels, k_i, and the kernels were then cross-correlated with the time series:

$$(t \star k)_j \equiv \sum_i t_i k_{i+j}. \qquad (7)$$

A positive peak in $(t \star k)_j$ indicates that the structure in the time series, t, is similar to that of the test kernel, k, when k is offset at position j. The detection threshold was set to $> +8\sigma_{t\star k}$, the limit at which real occultation events are expected to occur at a higher rate than false positives (see Section 3.7).

A suite of test kernels was selected to provide coverage over the distances, occulter sizes, and occultation impact parameters of interest in the cases being examined.

3. OCCULTATION SURVEY PARAMETERS

Using the methods described in Section 2, we now examine several observing parameters which are of importance in occultation work. Numerical simulations have been used to determine how these parameters influence the rate at which detectable occultation events occur. Whenever possible, optimal values are established.

We begin by determining the expected KBO occultation rate, and proceed to examine how it is effected by changes in the various observing parameters.

3.1. Expected KBO Occultation Rates

Existing estimates of the KBO occultation rate (R&M) were based on a single power law size distribution, which has since has been succeeded by a broken power law model (Kenyon & Bromley 2004; Pan & Sari 2005; Bernstein et al. 2004; Fuentes & Holman 2008; Fraser & Kavelaars 2009). Here, we evaluate the occultation rate expected for a KBO sky surface density based on the more recent broken power law model.

An occultation at distance, d [m], with maximum detectable impact parameter, b [m], projected velocity, v [m s^{-1}] (projected onto the plane perpendicular to the line of sight), and the sky surface density, Σ [deg^{-2}]; will occur at rate:

$$\mu = 2bv\Sigma \left(\frac{180}{\pi d}\right)^2 \quad [\text{s}^{-1}]. \qquad (8)$$

The Poisson probability of observing x occultations in time t is: $P(x) = [(\mu t)^x / x!] e^{-\mu t}$, and the expected time between occultations is (BKW):

$$t_{\text{exp}} = \frac{\ln|1 - P(x > 0)|}{-\mu}. \qquad (9)$$

Values of b, v, and Σ are determined as follows.

The relative perpendicular velocity of an occulter in an uninclined circular orbit is (Liang et al. 2002):

$$v = \left(\frac{\text{GM}_\odot}{r_\oplus}\right)^{\frac{1}{2}} \left[\left[\frac{r_\oplus}{r_o} \left(1 - \left(\frac{r_\oplus}{r_o}\right)^2 \sin^2(\varepsilon)\right) \right]^{\frac{1}{2}} + \cos(\varepsilon) \right], \qquad (10)$$

where $r_{\oplus,o}$ are the orbital radii of the Earth and occulter, ε is the solar elongation of the target star, and G and $M_\odot$ are the gravitational constant and solar mass.

We model the sky surface density, Σ, with the broken power law cumulative size distribution described by Gladman et al. (2001, eqs. 12 & 13). Known values have been expressed in a single constant of proportionality, Q_1.

$$\Sigma = Q_1 D_k^{q_S - 4.8} D_0^{1-q_S} \; [\text{deg}^{-2}], \quad Q_1 = 3.2 \times 10^8. \quad (11)$$

Here, D_0 [km] is the diameter of the smallest KBO considered, and D_k [km] is the diameter at which the power law breaks from the large object slope, $q_L = 4.8$ (Fraser & Kavelaars 2009; Fuentes & Holman 2008), to the small object collisional equilibrium slope q_S.

The widths of occultation shadows (the '2b' term in equation 9) take different values for smaller objects in the diffraction dominated regime, than for larger objects, for which such effects can safely be ignored. Nihei et al. (2007) define shadow width by the diameter of the Airy ring ($\sim 2\sqrt{3}\,\text{Fsu} = (6\lambda d)^{1/2}$), with a smooth transition between the two limiting cases:

$$W = \left[\left((6\lambda d)^{1/2}\right)^{3/2} + D^{3/2} \right]^{2/3} + 2R_\star. \qquad (12)$$

Simulations have shown this width is a reasonable estimate of the detectable width of an occultation (see for example, BKW, Figures 7 & 12). The cumulative surface density, Σ, includes objects larger than D, and a mean width, $\overline{W}$, was used to represent the average occulter.

$$2b = \overline{W} \approx \left[\left((6\lambda d)^{1/2}\right)^{3/2} + \overline{D}^{3/2} \right]^{2/3} + 2R_\star, \qquad (13)$$

where (derivation in Appendix B):

$$\overline{D}(D > D_0) = \frac{1}{N} \int_{D_0}^\infty \frac{dN(D)}{dD} D \; dD \qquad (14)$$

$$= \begin{cases} \left[\left(\frac{1-q_L}{2-q_L} - \frac{1-q_S}{2-q_S}\right) \left(\frac{D_0}{D_k}\right)^{q_S-2} \right. \\ \left. \quad + \; \frac{1-q_S}{2-q_S} \right] D_0. & (q_S \neq 2) \\ \left[\frac{1-q_L}{2-q_L} + \ln\left(\frac{D_k}{D_0}\right) \right] D_0 & (q_S = 2) \end{cases}$$

The fractional exponents 2/3 and 3/2 in equation 12 provide a smooth transition between terms, and the substitution of $\overline{D}$ to obtain $\overline{W}$ gives a reliable first order approximation[2].

Times required to observe one or more occultations by $D > D_0$ objects are shown in Figure 4 for optical ($\lambda = 550$nm) and X-ray ($\lambda = 0.4$nm) light (the bands observed in occultation searches to date). The expected average times between events are shown (equation 9 with $P(x > 0)$=0.68, or 68% confidence for one or more events). Curves were computed for q_S=2.0 (Fuentes & Holman 2008; Fraser & Kavelaars 2009), and 3.0. Other parameter values were: $R_\star$=0 (point source), distance d=40 AU, solar elongation ε=180° (opposition), D_k=50km (Bernstein et al. 2004), and q_L=4.8 (Fraser & Kavelaars 2009).

---

[2] As W is not a linear function of D, $\overline{D}$ cannot be directly substituted for D to obtain $\overline{W}$ (as in equation 13). However, to a first-order approximation, W *is* a linear function of D, and the substitution is valid as an approximation.
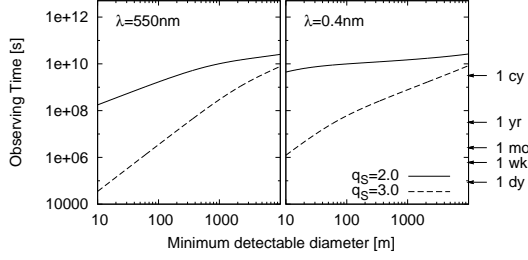
FIG. 4.— Average time between occultations for KBO occultation searches performed in the optical (left) and X-ray (right). Different curves represent different possible slopes for the small object size distribution, q_S. The waiting times required for 95% confidence are $-\ln|0.05| \approx 3\times$ longer (equation 9) than the average values shown here.

The 95% confidence times may be more appropriate estimates for programs seeking to detect a single event. From equation 9, these are $-\ln|0.05| \approx 3\times$ longer.

The expected occultation rates are similar for X-ray and optical observations. Although the X-ray Fresnel scale is small enough to offer access to the more-numerous 10m-sized objects, there is only a single bright ecliptic X-ray target (Sco X-1). The relative abundance of suitable optical targets (eg. M35, with 100s of upper main sequence stars) makes them a better choice for a large scale KBO occultation survey.

3.2. *Nyquist Sampling for a Diffraction-Dominated Occultation Event*

A measured signal should be sampled at a frequency, f_s, which is $2\times$ the Nyquist frequency, f_{Ny} (highest frequency to be represented). A diffraction-dominated occultation event contains some power at all frequencies, and the Nyquist frequency is defined here to be the sampling rate for which 95% of the cumulative power is present in frequencies below f_{Ny}. This limit is, and must be, somewhat arbitrary. The goal was to identify an upper limit for which the overwhelming majority of the occultation signal strength would be represented in the sampled measurements. The validity of this 95%-power limit is supported by numerical tests which are presented in Section 3.4.

Power-spectra were computed for the lightcurves of r_{KBO}=0.1, 0.3, and 1.0 Fsu occulters. The Fresnel-scale unit is a function of wavelength, λ, and integration over a passband was simulated by averaging lightcurves within $r_{KBO}\pm15\%$ (eg. $0.085 < r_{KBO} < 0.115$ for $r_{KBO} = 0.1$ Fsu). This $r_{KBO} \pm 15\%$ range simulates integration over a $\lambda\pm27\%$ passband, and was chosen to represent the 400-700 nm passband of visible light. The lightcurves, power spectra, and cumulative power spectra are shown in Figure 5. Conveniently, the cumulative power reaches 95% at a wave number of k=1 Fsu^{-1}, regardless of r_{KBO}, corresponding to a Nyquist-sampled sampling rate of f_s=2 Fsu^{-1}.

The lack of dependence on r_{KBO} would not generally be the case for $r_{KBO} \ll 1$ Fsu lightcurves observed in monochromatic light. A significant portion of the power would then be present in extended high-frequency ringing. When a realistic integration over a passband is considered, the extended ringing cancels and the f_{Ny}= 1 Fsu limit is valid, even for the $r_{KBO} = 0.1$ Fsu example shown in Figure 5.
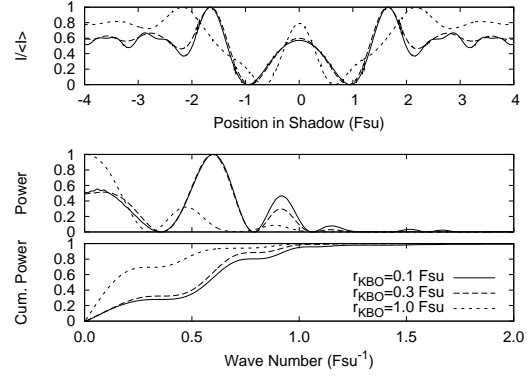

FIG. 5.— Diffraction-dominated occultation profiles (top) and the corresponding power spectra (middle), and cumulative power (bottom). The cumulative power reaches 95% at a frequency $f_{Ny} < 1$ Fsu^{-1}, and Nyquist sampling is achieved at a sampling rate $f_s = 2$ Fsu^{-1}.

For visible-light observations (λ=400-700 nm) of KBOs at distance d=40 AU, an occultation with a projected velocity of v=26 km s^{-1} (ie. at solar opposition) would be Nyquist sampled at:

$$f_s = 2 \text{ Fsu}^{-1} \cdot \left(\frac{v}{(\lambda d/2)^{1/2}} \right) \text{ Fsu s}^{-1} \qquad (15)$$

$$= 40 \text{ s}^{-1}.$$

Beyond 40 AU, the projected velocity asymptotically approaches 30 km s^{-1}, and the sampling rate scales as $f_s \propto d^{-1/2}$ until the projected size of the target star is comparable to the Fresnel scale.

3.3. *Solar Elongation of the Target Star*

Occultations observed off-opposition have lower relative velocities perpendicular to the line of sight, and are better-sampled events. But, they are less probable events as the occultation rate increases linearly with velocity, $\mu = 2bv\Sigma$ (equation 8). Here, we determine how the combination of increased detectability and decreased event probability effect the observed occultation event rate as a function of solar elongation.

Diffraction dominated occultation profiles were generated for 50 logarithmically-spaced circular occulters with sizes 100 m $< r_{KBO} < $ 2000 m, at 40 AU, observed in optical light (400–700 nm). The circular occulting masks were assembled out of rectangular masks (Roques et al. 1987; BKW), and target stars were assumed to be point sources.

Artificial time series were generated with 1% 1/f noise (S/N = 100), as described in Section 2.2. Tests were also performed with noise levels of 2% and 4%, and gave similar results. Time series had 65536 points, and were tested with sampling rates of 10 s^{-1}, 20 s^{-1}, 40 s^{-1}, and 80 s^{-1} (above and below the Nyquist limit described in Section 3.2).

Relative velocities were computed at solar elongations between opposition and the stationary point (100 - 180° in increments of 5°), and the template diffraction patterns were scaled to produce templates corresponding to each velocity. The scaled templates were sampled at the rates listed above and 10 simulated events were planted in the time series. This was repeated for 30 evenly-spaced

occultation impact parameters extending to 8× the Fresnel scale. The planting process is described in BKW.

The Cross-correlation detection algorithm was used to attempt detection of planted events (Section 2.3), and the fraction of recovered events transitioned between ∼1 for large, easily detected events, and 0 for events well below the detection threshold. The occultation rate was integrated by summing contributions from each δr radius bin: $\delta\mu = 2b_{\max}(r)v\delta\Sigma(r,q_S)$, where $b_{\max}$ was the maximum impact parameter detected, and $\delta\Sigma(r,q_S)$ was the sky surface density of objects in the size range $r < r_{KBO} < r+\delta r$, for a size distribution having a small-object slope of q_S. Slopes of q_S=2, and 3 were tested. The integral was truncated to exclude objects with $r_{KBO} > 2$ km as the sky surface density of objects larger than this is comparatively extremely small for the size distribution slopes tested. The occultation rates were normalized to the solar opposition value and are shown in Figure 6. Results of the q_S=3 tests were similar those for q_S=2, and are not presented in Figure 6.
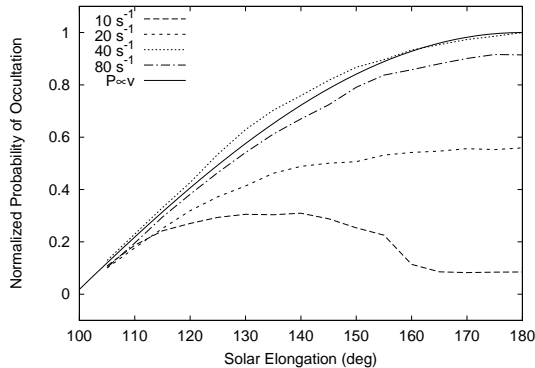

FIG. 6.— The relative detectable occultation rate as a function of solar elongation (normalized to an elongation of 180°) for 10, 20, 40, and 80 s^{-1} sampling rates. The reduction of D$_{\min}$ (Figure 7) gives some off-opposition benefit for sub-Nyquist sampling rates $\lesssim$40 s^{-1}. Events are sufficiently sampled at $\gtrsim$40 s^{-1}, and any such advantage is lost.

The limiting size, $D_{\min}$, was defined to be the diameter at which the shadow width, $2b$, reached 1 Fsu. This was found to be a robust measure of the diameter at which an object was too small to be detected. The minimum detectable sizes versus solar elongation are shown in Figure 7. They were found to decrease as a function of solar elongation for the sub-Nyquist samplings (10 s^{-1} and 20 s^{-1}), but did not change significantly at the higher sampling rates.

The improved off-opposition detectability of the more numerous smaller objects in the 10 s^{-1} and 20 s^{-1} tests suggests that detection rates in such an observing program would not decrease in proportion to v. Above the Nyquist sampling rate, the detection rate decreases in proportion to v, and no improvement in detectability is achieved by working off-opposition.

3.4. *Sampling Effects*

The Nyquist limit presented in Section 3.2 indicates that the theoretical optimum sampling rate is f_s=2 Fsu^{-1}. Here we examine the detection rate for occultation events observed by a camera operating at different sampling rates.
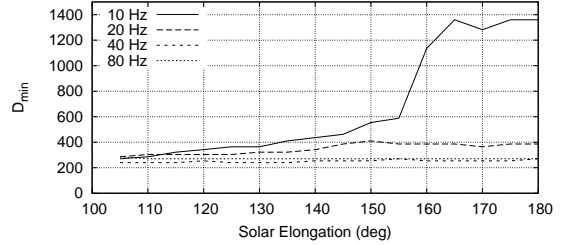

FIG. 7.— The minimum detectable size as a function of solar elongation. The improved event sampling due to lower relative velocities allows detection of smaller objects for $f_s < 20$ s^{-1}, but has little effect at higher sampling rates.

Occultation profiles and artificial time series were generated as described in Section 3.3. Our $1/f$ noise model was only tested for sampling up to 40 s^{-1} (the sampling rate of our observed time series). The $1/f$ property of scintillation must ultimately transition to (white) photon noise at $\gtrsim 100$s^{-1} (Dravins et al. 1997). Our time series were therefore simulated with Poisson variates (white noise) to overcome this limitation in our understanding of the noise beyond 40 s^{-1}. Though each test was performed with Poisson variates, it was repeated with the $1/f$ noise model for frequencies up to $f = 40$ s^{-1}, and results were found to be consistent with the Poisson results for the range of frequencies tested. This simulation represents space-based observations very well, and is representative of ground-based observations up to $f = 40$ s^{-1}.

Constant values of D=40 AU (ie. KBOs), and q_S=2.0 were used, and the sampling rate, f, of the camera was varied in logarithmic spacings 6 s^{-1} < f < 600 s^{-1}. The tests were bench-marked with respect to a sampling-specific signal to noise, S/N$_f$. A bench mark sampling rate of $f = 40$ s^{-1} was used, and signal to noise ratios of S/N$_{40}$=100, 50, 25 were tested. At each sampling rate Poisson variates were drawn to represent fluxes, $I_i(f)$, with mean $\overline{I}(f)$ (in photo-electrons):

$$\overline{I}(f) = \left(\frac{40}{f}\right)(\text{S/N}_{40})^2. \qquad (16)$$

Target stars for occultation work are generally bright (V<12 mag) and sky noise was not considered.

Simulated occultation events were planted in the data, and random Gaussian variates, $R_i(f)$, with a mean, $\overline{R}(f)$=0, and standard deviation, $\sigma_R(f)$, were then added to each point in the time series to simulate read noise. Read noise is a function of the clamp-and-sample time for a pixel, $t_{CS}^{-1/2}$, (McLean 1997). The value, $\sigma_R(f)$, at each sample rate, f, was normalized to the 40 s^{-1} value, $\sigma_R(40)$:

$$\sigma_R(f) = \sigma_R(40)\left(\frac{f}{40}\right)^{1/2}. \qquad (17)$$

It was assumed that t_{CS} is linearly related to the full read-out time for the CCD. This is consistent with a constant-size region of a frame transfer device being read out at a rate which makes full use of the exposure time. The dead-time associated with frame transfer is typically 1 ms and was not considered. Values of $\sigma_R(40)$=0, and 15 e$^-$ were tested.

The photon noise plus read noise signals, $I_i(f) + R_i(f)$, were searched for the planted occultation events with the cross-correlation detection algorithm, and the smallest detectable size, D_{min}, was determined as described in Section 3.3. The density, Σ, of occulters larger than D_{min} was computed for a small object slope $q_S=2$ (equation 11), and the probability of occultation was integrated over the KBO radii as described in Section 3.3.

The detection probabilities at different sampling rates are presented in Figure 8. The presence of read noise does not strongly influence the occultation probability when the photon noise is low (upper panel), but becomes a significant attenuating factor at higher photon noise levels (lower panel). This is not surprising as the read noise is a more significant component of the total noise level when photon counts are low.
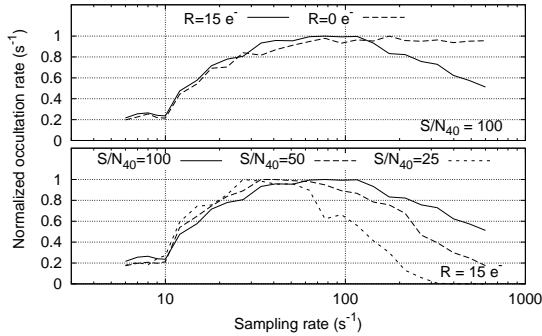

FIG. 8.— The detectable occultation rate (normalized to peak value) as a function of the sampling rate. Both the influence of read noise (top) and that of photon noise (bottom) are shown. In each case, detectability peaks at the theoretical $f_s = 40$ s^{-1} rate predicted in Section 3.2. The presence of read noise reduces the detection probability at high sampling rates, and the effect becomes more pronounced at low signal to noise.

3.5. Signal to Noise

Significant increases in the occultation event rate can be achieved by using a larger telescope to increase the signal to noise in the photometric time series. Here, we evaluate the detectable occultation rate at different photometric noise levels which are representative of available observing facilities.

KBO (ie. 40 AU) occultation profiles were planted in simulated 40 s^{-1} (ie. optimally sampled) time series containing $1/f$ noise at logarithmically-spaced signal to noise levels of $10 < \text{S/N} < 10000$. Detection was attempted with the cross-correlation algorithm to determine the minimum detectable size, D_{min}, as described in Section 3.3. Figure 9 shows D_{min} versus S/N.

The minimum diameter, in Fsu, empirically follows the power law:

$$D_{min} = Q_2 \ (S/N)^{-\eta}, \qquad (18)$$

with $Q_2 = 3.2 \pm 0.2$, and $\eta = 0.52 \pm 0.01$ (by linear least-squares fit to $\log D_{min} = \log Q_2 - \eta \log(S/N)$). This relation was found to remain valid when tested at different distances, but is expected to break down at distances for which the target star has a projected radius $\gtrsim 1$ Fsu. Combining the minimum detectable size with the
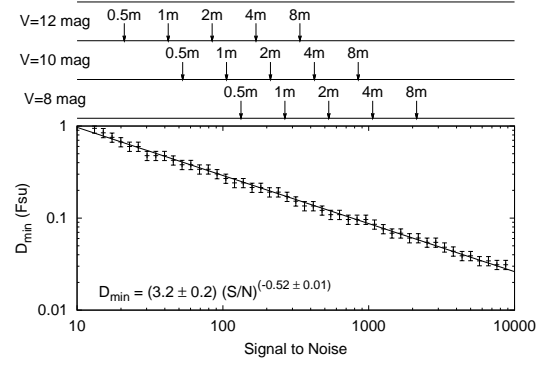

FIG. 9.— The minimum detectable size as a function of the photometric signal to noise. The telescope apertures required to achieve the S/N values presented are shown above for V=8, 10, and 12 mag target stars.

cumulative size distribution for the small occulters (equation 11) the sky surface density, Σ, can be expressed in terms of S/N:

$$\Sigma = Q_1 \ Q_2^{1-q_S} \ D_k^{q_S - 4.8} \ (S/N)^{-\eta \ (1-q_S)}. \qquad (19)$$

The telescope apertures required to obtain the corresponding S/N values for apparent magnitudes of V=8, 10, and 12 mag[3] are shown above the figure for reference.

3.6. Size-Distance Degeneracy and the Main Belt Occultation Rate

Similar sized objects (in Fsu) at different distances will produce diffraction profiles that are scaled in width with respect to one another. This makes it possible for distant and nearby occulters to produce identical occultation lightcurves; a distant occulter will cast a wider shadow but the observer will move through it more quickly. Here, we demonstrate how such a size/distance conspiracy manifests itself observationally, and the possibility of degeneracy with the Main Belt Asteroids (MBAs) is considered.

A diffraction-dominated occultation will have a peak-to-peak width of $(6\lambda d)^{1/2} \approx 3.5$ Fsu (Nihei et al. 2007). The duration of an occultation observed at wavelength, λ, for an occulter at distance, d, can be expressed as:

$$t_{occ} = \frac{(6\lambda d)^{1/2}}{v_\perp}, \qquad (20)$$

where $v_\perp$ is the perpendicular velocity of the occulter described by equation 10, and the distance to the occulter is given by:

$$d = \left[r_\oplus^2 + r_o^2 + 2r_\oplus r_o \cos\left(\varepsilon + \sin^{-1}\left(\frac{\sin(\varepsilon)}{r_o} \right) \right) \right]^{1/2}. \qquad (21)$$

Here, $r_{\oplus,o}$ are the Earth-Sun and occulter-Sun distances, and ε is the solar elongation of the target star.

Figure 10 shows occultation time as a function of the distance to the occulter for targets at different solar elongations. At opposition, a diffraction-dominated occultation by an object at 40 AU produces a shadow width

---

[3] Through-put of 0.65 was used to account for quantum efficiency (0.85), mirror reflectivity and transparency of optics (0.85), and atmospheric transparency (0.9).

similar to that observed for an occultation by an object
at 0.08 AU, just outside of Earth's orbit. The nearby ob-
ject would have to have the same size, in Fsu, to project
a shadow with the same structure; and the ratio of sizes
is given by the ratio of Fresnel scales at the two distances:
$(0.08/40)^{1/2} = 0.045$. Thus, a 500m diameter KBO at
40 AU will produce an occultation shadow identical to
that produced by a 0.045×500 m = 22m diameter ob-
ject at a 0.08 AU. This is the only degenerate point for
$\varepsilon = 180°$; all other objects at all other distances will pro-
duce shadows which are different in either duration or
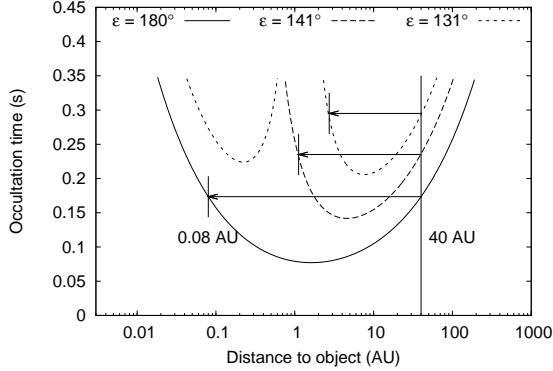amplitude.

FIG. 10.— The duration of occultation as a function of the
distance to the occulter. Different curves represent observations
made at different solar elongations. Degeneracy of size/distance
occurs within the Main Belt for elongations $131° \lesssim \varepsilon \lesssim 141°$.

The degenerate point moves to greater distances when
$\varepsilon \neq 180$. The greatest risk of degeneracy occurs when the
degenerate point is within the asteroid belt ($\sim 2.0 - 3.5$
AU). This occurs when a target is observed at elongations
$131° \lesssim \varepsilon \lesssim 141°$. For elongations $\varepsilon < 133°$, a second set
of degenerate points enters the parameter space. These
points represent possible prograde occultations, as the
elongation has moved beyond the stationary point for
the distance in question. The second set of degeneracy
points lies within the Main Belt for elongations $116° \lesssim
\varepsilon \lesssim 125°$.

At $\varepsilon \approx 136°$, the degeneracy point is within the Main
Asteroid Belt at distance $d = 1.7$ AU (orbital radius 2.5
AU). There, a 500 m KBO would be degenerate with a
$(1.7\text{AU}/40\text{AU})^{1/2} \times 500$ m = 104 m MBA.

To estimate the number of conflicting occulters we
compute the ratio $P_{\text{MBA}}/P_{\text{KBO}}$, with $P = 2bv\Sigma$ (equa-
tion 8). The shadow widths, $2b$, were taken to be 3.5
Fsu (equation 12), and velocities were computed with
equation 10. KBO sky surface densities were calculated
with equation 11, and MBA sky surface densities were
converted from the power law model of the cumulative
luminosity function (CLF) for the Main Belt with slope
$\alpha = 0.27$ (Gladman et al. 2009, in preparation) :

$$\Sigma(< m_{\text{R}}) = 210 \times 10^{\alpha \, (m_{\text{R}}-23)}, \quad 20 < m_{\text{R}} < 23. \quad (22)$$

When an object with diameter D, albedo $p = 0.05$,
and heliocentric distance Δ is observed in reflected light
at phase angle $\beta = \arcsin(d\sin(\varepsilon)/\Delta)$ (Sine Law) at a
distance d from the Earth, its apparent V magnitude is
(Cox 2000):

$$V = H(\beta) + 5\log(d\Delta), \quad (23)$$
$$H(\beta) = H - 2.5\log[(1-G)\Phi_1(\beta) + G\Phi_2(\beta)], \quad (24)$$
$$\Phi_i = \exp[-A_i[\tan(\beta/2)]^{B_i}], \quad (25)$$
$$H = 15.645 - 2.5\log p - 5\log D. \quad (26)$$

The constant terms have values: $A_1 = 3.33$, $A_2 = 1.87$,
$B_1 = 0.63$, and $B_2 = 1.22$; and a slope parameter of $G =
0.2$ (typical for MBAs) was used. A value of V–R=0.4
(typical for MBAs) was then used to obtain apparent R
magnitudes to apply in equation 22.

The size distributions of both the KBO and MBA pop-
ulations are modeled as power laws, and the probability
ratio, $P_{\text{MBA}}/P_{\text{KBO}}$, remains constant as a function of
size, D, when the slopes are equal: $q_{\text{S}} = 5\alpha + 1 = 2.35$.
In this case the probability ratio is $P_{\text{MBA}}/P_{\text{KBO}} = 2.5$,
and occultations by MBAs are expected to be more nu-
merous. If $q_{\text{S}} < 2.35$ for the Kuiper Belt, occultation
events will be predominantly by Main Belt occulters.

Via this transformation, a 100 m MBA has magnitude
$m_{\text{R}} = 26.6$ mag, and is an extrapolation of ~ 3.6 magni-
tudes beyond the observed limit of the CLF (Gladman
et al. 2009, in preparation) The assessment remains valid
for MBAs with sizes $D_{\text{MBA}} \gtrsim 500$ m, and $D_{\text{KBO}} \gtrsim 2500$
m.

3.6.1. *Breaking the Size-Distance Degeneracy*

As the slopes for the size distributions of small KBOs
and MBAs are not well understood, it is worthwhile to
examine a method of breaking the size-distance degener-
acy.

In an occultation survey, a target star with large pro-
jected diameter is undesirable as it causes deterioration
of the diffraction profile. This deterioration could allow
a shadow cast by a distant occulting object to be distin-
guished from its near-field degenerate counterpart. De-
terioration of a profile due to the size of the background
star becomes significant when the star's radius is com-
parable to the Fresnel scale. The Fresnel scale increases
as the square-root of the distance, but the projected size
of the background star increases linearly with distance
to the occulter. Thus, a star which has a 'large' (~ 1
Fsu) projected size at 40 AU has a relatively small (~ 0.3
Fsu) projected size at 1.7 AU. The ideal target star to
break the degeneracy will be the brightest available with
a projected diameter of ~ 1 Fsu.

3.7. *False Positives*

The diffraction-dominated occultation shadows being
sought in a photometric time series can be similar in
structure to the noise, and random statistical fluctua-
tions could be misidentified as occultations. Here we
evaluate the false positive rate with our cross-correlation
detection algorithm, and compare it to the expected
occultation rate to determine an appropriate detection
threshold.

Artificial time series were generated with different
noise properties (S/N, and power-spectral slope), and the
cross-correlation detection algorithm was run on the sim-
ulated data. Three hundred detection kernels for a point-
source with 50m $< r_{\text{KBO}} < 1200$m, 10AU $< d_{\text{KBO}} <
160$AU, and $b < 3$ Fsu (BKW) were used. Each time
series had length $2^{23} \approx 8.4 \times 10^6$ points (58.2 hours at

40 s^{-1} sampling) and was guaranteed not to contain any real occultation events. The distribution of false positive events in standard deviation units is presented in Figure 11 with the expected Gaussian distribution for reference.
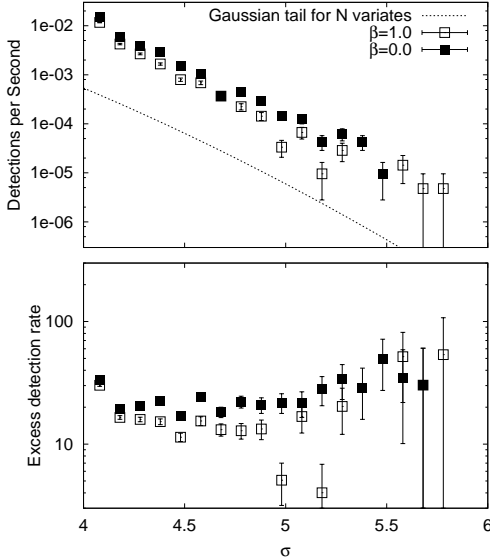

FIG. 11.— The distribution of false positives in units of standard deviations shown in events per second (top), and as a fractional excess above the rate expected for Gaussian variates (bottom). The use of multiple detection kernels causes the number of false positives to be $\sim 10-20\times$ higher than the rate expected for Gaussian variates. Changes in the signal to noise do not significantly alter the rates, but changing the slope of the power spectrum from -1 (1/f noise) to 0 (Poisson noise) increased rates by a factor of ~ 2.

The cross-correlation detections are $\sim$10-20$\times$ more common at all levels of significance because multiple detection kernels were used. But, the false positive rate did not increase by a factor of 300 (the number of kernels) because the kernels do not represent independent tests. By design, the spacing of kernel parameters r_{KBO}, d_{KBO}, and b was chosen to allow an event to be detected by multiple kernels.

The false positive rate decreases as the slope of the power spectrum becomes steeper. An occultation lightcurve has a peak in power at ~ 0.5 Fsu (see Figure 5), and a negative slope in the power spectrum indicates that more power is present in the lower frequencies. The relative amount of power in the noise band shared by occultation events decreases as the slope of the power spectrum steepens, and fewer false positives are observed.

Evaluation of the false positive rate must be done on a per-observation basis with an accurate model of the photometric noise, and with the same detection algorithm used on the real data. An excess of false positives above the Gaussian estimate will be produced by any method in which multiple passes are made over the data to extract different patterns. In the example presented (Figure 11), reference to an '$n - \sigma$' cross-correlation peak would be valid for the kernel tested, but would be a misleading representation of the statistical significance for the complete collection of kernels.

3.7.1. *Selection of a Detection Threshold*

There is no established detection threshold above which an event should be considered a viable candidate. We have used 8σ throughout this work and will now offer a justification for that limit.

False positive events should represent a small portion of the number of observed events, e.g. 5% for 2σ confidence. To determine a detection threshold, we consider the ratio of expected genuine events to false positives events as a function of statistical significance (in standard deviation units).

The false positive event rate, μ_{fp}, was computed by scaling the amplitude of a Gaussian to fit the false positive distribution shown in Figure 11. The scaling compensates for the increased false positive rate produced by the cross-correlation with multiple kernels.

The expected occultation rate at each level of statistical significance was estimated with a plant/recover process for a comprehensive selection of KBOs. Occultation profiles were tested for KBOs at 40 AU, observed in visible light, with radii 10 m $< r_{KBO} <$ 2000 m (n=200, $\delta r_{KBO} = 10$ m), and impact parameters 0 m $< b <$ 8000 m (n=100, $\delta b = 341$ m). The statistical significance of the selected events was measured in artificial 40 s^{-1} time series with S/N=25,100 and β=1.0 (1/f noise), and the occultation rate for each grid point was calculated:

$$\delta\mu(r_i, b_j) = 2\ \delta b\ v\ \left[\Sigma(r_i - \delta r/2) - \Sigma(r_i + \delta r/2)\right]. \quad (27)$$

Each grid point was binned in statistical significance, and the rates, $\delta\mu$, were summed in each of the bins:

$$\mu(\sigma_k) = \sum_{i,j} \delta P(r_i, b_j), \quad (\sigma - \delta\sigma/2 < \sigma_k < \sigma + \delta\sigma/2).$$
$$(28)$$

The occultation rates for false positives, $\mu_{fp}(\sigma_k)$, and expected genuine positives, $\mu(\sigma_k)$, are shown in Figure 12 (upper panel) for different slopes of the KBO size distribution, q_S=2,3. The ratio of the rates, $\mu(\sigma_k) : \mu_{fp}(\sigma_k)$, is shown in the lower panel.

Variability in the expected occultation rate is due almost entirely to uncertainty in the slope of the size distribution, q_S (factors of $\gtrsim 100\times$ versus $\lesssim 10\times$ for changes in S/N).

From Figure 12, we see that the expected genuine occultation rate exceeds the false positive rate for statistical significances of $\gtrsim 7\sigma$ (q_S=3), or $\gtrsim 8\sigma$ (q_S=2). A limit of 8σ has been used throughout this work.

If the photometric noise properties are sufficiently well understood, the distribution of false positives can be modeled with artificial time series. It would then be possible to infer the presence of genuine events as a statistical excess among more numerous false positives.

4. DISCUSSION

The parameter space for occultation studies is vast, including properties of the occulter (size, distance, sky surface density), the target star (solar elongation, projected diameter), the time series (sampling rate, S/N, power spectrum slope), and the stochastic nature of the event itself (impact parameter). We have endeavored to reduce the complexity of this parameter space and determine optimum values for those parameters which are under an observer's control. Here, we discuss other considerations associated with SSO work.
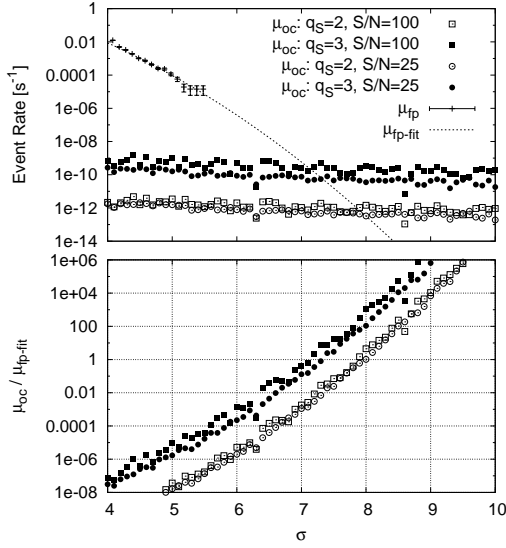
FIG. 12.— The distributions of false and genuine positive occultation events in units of standard deviation (top), and the ratios of real-to-false positive events (bottom). False positives dominate for significance of $\lesssim 8\sigma$.

The plant and recover method was adopted for a variety of tests performed, and used the same occultation profile for planting as was used for construction of the detection kernel. When used for detection in real data, multiple kernels are used to cover the parameter space of interest. The parameters of an occultation event ($r_{\rm KBO}$, $d_{\rm KBO}$, and b) would not be expected to match any of the kernels exactly, but would be recovered due to overlap in their ranges of sensitivity. Use of the same profile for both planting and detection improved the efficiency of our testing code, but does not compromise the validity of any results.

Our finding that occultation events are best sampled at f_s=2 Fsu^{-1} is based on 95% of the cumulative power being in frequencies below $f_{\rm Ny}$=1 Fsu^{-1}. This is true only for diffraction profiles integrated over a range of wavelengths. An occultation profile observed in monochromatic light will contain extended ringing and retain considerable power at frequencies beyond 1 Fsu^{-1}. The sampling rate we provide here is valid for filters with $\sim$ 100 nm pass-bands, typical of broad-band filters used in optical astronomy.

Estimates of the occultation rate as a function of the sampling rate were based on plant/recover tests in time series of Poisson variates rather than $1/f$ noise. Our photometric time series were sampled at 40 s^{-1} and we did not extrapolate the power spectrum to higher frequencies in order to simulate the noise at higher sampling rates. The tests were repeated with $1/f$ time series for frequencies up to f=40 s^{-1}, and these were found to be consistent with the Poisson noise tests for the range of frequencies compared.

The detectable occultation rates shown in Figure 4 are considerably lower than earlier estimates. An occultation by a $D \approx$1000 m object would be expected at a rate of $\mu = 10^{-8} - 10^{-10}$ s^{-1}, where the previous rate was 5×10^{-7} s^{-1} (R&M). The rates presented here take into account a break in the size distribution which was not well established when earlier estimates were made. The

break to a shallower size distribution at $r_{\rm KBO} \sim 25$ km dramatically reduces the expected sky surface density of km-sized KBOs.

The cross-correlation detection algorithm was used in an occultation search of 40 s^{-1} photometric time series from two B9V stars in M35 (BKW). In real photometric time series, false positives were detected at a higher rate than would be predicted in Section 3.7 of this work. The critical difference between observed and simulated time series is that photometric stability cannot be maintained for an observed time series. Atmospheric transparency can change on time scales of a few minutes, and thereby change the signal to noise ratio of the photometry. To guard against this, detection algorithms should normalize a candidate event's statistical significance by a more local measure of the standard deviation than has been used in the past – within seconds, rather than minutes of a candidate point.

5. SUMMARY

We have provided a comprehensive assessment of the various observing parameters relevant in an SSO survey. Our aim has been to identify optimal values for parameters to guide future observations in this field. The results we have obtained are summarized here.

- We have estimated occultation event rates based on a broken power law size distribution, and found rates of $10^{-8} - 10^{-10}$ s^{-1} for km-sized objects. The variability is due to the large uncertainty in the size distribution slope, $q_{\rm S}$, for small objects.

- Fourier analysis indicates that 95% of the cumulative power in the power spectrum of a $\lambda = 400 - 700$ nm occultation profile is present in frequencies of $f \lesssim 1$ Fsu^{-1}, indicating that an event can be critically (Nyquist) sampled at a rate of f_s=2 Fsu^{-1}. To probe the Kuiper Belt at 40 AU, this corresponds to a sampling rate of 40 s^{-1}. Numerical tests of the sampling rate indicate that sampling significantly above the Nyquist limit ($\gtrsim$80-100 s^{-1}) increases read-noise, and reduces the detectable KBO occultation rate.

- The photometric noise present in 40 s^{-1} ground-based observations has a power spectrum with the form $1/f^\beta$, with $\beta \approx 1$. We have used Fourier methods to generate $1/f$ noise artificially and simulate realistic photometric time series. Plant-and-recover tests were performed with these time series to numerically test various modes of observation.

- When optimally sampling, the detectable occultation event rate is maximized by observing a target at solar opposition (within $\pm 20 - 30°$). Observing off-opposition does not significantly improve detectability of smaller, more numerous objects unless the sampling rate of the camera is sub-critical for an observation at opposition.

- In a diffraction-dominated occultation event which is well sampled, the occulter distance will manifests itself in the width (duration) of the event. A given distance is degenerate with either one, or three others, depending on the solar elongation of the observation. Occultation events by KBOs at 40 AU are

degenerate with 2.0–3.5 AU MBAs for observations performed at elongations of $116° \lesssim \varepsilon \lesssim 125°$, or $131° \lesssim \varepsilon \lesssim 141°$.

- Occultations by MBAs may occur at a rate comparable to those for KBOs depending on the slopes of the size distributions for the two populations. An MBA occultation observed at solar opposition will be $\sim 0.5\times$ the duration of a KBO event, and the two should be distinguishable. The sampling rate adopted for a survey targeting multiple distances should be the highest of the critical sampling rates for each individual distance (~ 80 s^{-1} for MBAs).

- Due to the expected rarity of KBO occultation events, false positives are likely to be more common than real events for levels of statistical significance $\lesssim 7 - 8\sigma$, depending on the slope of the KBO size distribution.

APPENDIX

DERIVATION OF THE $1/F$-NOISE NORMALIZATION CONSTANT

The normalization constant, A (equations 2, and 3) is need to produce an artificial time series with $1/f$ scintillation-like properties. With variables as defined by equations 2 through 5 in Section 2.2.2, the value of A can be determined as follows:

Taking the time variate $h_k = \overline{h} + \varepsilon_k$ ($\overline{\varepsilon} \equiv 0$, $\sigma_\varepsilon \equiv \sigma_h$), substitution of equation 5 into Parseval's theorem yields:

$$\sum_{k=0}^{N-1} |h_k|^2 = \frac{1}{N} \sum_{n=0}^{N-1} |H_n|^2, \tag{A1}$$

$$\sum_{k=0}^{N-1} (\overline{h} + \varepsilon_k)^2 = \frac{1}{N} \left[H_0^2 + \sum_{n=1}^{N-1} (A f_n^{\beta/2} a_n)^2 \right],$$

$$\sum_{k=0}^{N-1} \overline{h}^2 + \sum_{k=0}^{N-1} 2\overline{h}\varepsilon_k + \sum_{k=0}^{N-1} \varepsilon_k^2 = \frac{1}{N} \left[H_0^2 + A^2 \sum_{n=1}^{N-1} f_n^\beta a_n^2 \right],$$

$$N^2 \overline{h}^2 + 2\overline{h} N^2 \overline{\varepsilon} + N^2 \sigma_h^2 = H_0^2 + A^2 \sum_{n=1}^{N-1} f_n^\beta a_n^2,$$

$$A = N\sigma_h \left[\sum_{n=0}^{N-1} f_n^\beta a_n^2 \right]^{-1/2}.$$

THE AVERAGE OBJECT DIAMETER IN A BROKEN POWER LAW SIZE DISTRIBUTION

Equation 14 describes the average diameter of an object in a broken power law size distribution. The expression can be derived as follows:

$$\overline{D} = \frac{1}{N} \int_{D_0}^{\infty} \frac{dN(D)}{dD} D \, dD = \frac{1}{N} \left[\int_{D_0}^{D_k} \frac{dN(D < D_k)}{dD} D \, dD + \int_{D_k}^{\infty} \frac{dN(D > D_k)}{dD} D \, dD \right], \tag{B1}$$

where N is as defined in equation **??**. These two integrals can be expressed as:

$$\int_{D_0}^{D_k} \frac{dN(D < D_k)}{dD} D \, dD = \int_{D_0}^{D_k} \left[\frac{A(r_{max}^{1-c} - r_{min}^{1-c})}{(1-c)(q_L - 1)} D_k^{q_S - q_L} \left((1 - q_S) D^{-q_S} \right) \right] D \, dD,$$

$$= \frac{A(r_{max}^{1-c} - r_{min}^{1-c})}{(1-c)(q_L - 1)} D_k^{q_S - q_L} \frac{\left[(1 - q_S) \left(D_k^{2-q_S} - D_o^{2-q_S} \right) \right]}{2 - q_S}, \tag{B2}$$

and

$$\int_{D_0}^{D_k} \frac{dN(D > D_k)}{dD} D \, dD = \int_{D_k}^{\infty} \left[\frac{A(r_{max}^{1-c} - r_{min}^{1-c})}{(1-c)(q_L - 1)} \left((1 - q_L) D^{-q_L} \right) \right] D_k \, dD,$$

$$= \frac{A(r_{\max}^{1-c} - r_{\min}^{1-c})}{(1-c)} \frac{D^{2-q_{\mathrm{L}}}}{q_{\mathrm{L}} - 2}. \tag{B3}$$

With substituting of equations B2, and B3, equation B1 can be reduced to give:

$$\overline{D}(q_{\mathrm{S}}, q_{\mathrm{L}} \neq 2) = \left[\left(\frac{1-q_{\mathrm{L}}}{2-q_{\mathrm{L}}} - \frac{1-q_{\mathrm{S}}}{2-q_{\mathrm{S}}} \right) \left(\frac{D_0}{D_k} \right)^{q_{\mathrm{S}}-2} + \frac{1-q_{\mathrm{S}}}{2-q_{\mathrm{S}}} \right] D_0, \qquad D_0 < D_k. \tag{B4}$$

Equation B4 is undefined for $q_{\mathrm{L}} = 2$, but this is well below current estimates of its value ($q_{\mathrm{L}} \approx 4.8$ Fuentes & Holman 2008; Fraser & Kavelaars 2009). The equation, as shown, is also undefined for $q_{\mathrm{S}} = 2$, but has a finite limiting value. It can then be rearranged to isolate the $(q_{\mathrm{S}} - 2)$ terms, and take the limit as $q_{\mathrm{S}} \to 2$:

$$\overline{D}(q_{\mathrm{S}} = 2) = \lim_{q_{\mathrm{S}} \to 2} \left[\left(\frac{1-q_{\mathrm{L}}}{2-q_{\mathrm{L}}} \left(\frac{D_0}{D_k} \right)^{q_{\mathrm{S}}-2} + (1-q_{\mathrm{S}}) \left(\frac{1 - (D_0/D_k)^{q_{\mathrm{S}}-2}}{2-q_{\mathrm{S}}} \right) \right) \right] D_0. \tag{B5}$$

The limit can then be computed with L'Hopital's rule by taking derivatives of the numerator, $(1 - (D_0/D_k)^{q_{\mathrm{S}}-2})$, and denominator, $(2 - q_{\mathrm{S}})$, in the second term of Equation B5:

$$\overline{D}(q_{\mathrm{S}} = 2) = \left[\left(\frac{1-q_{\mathrm{L}}}{2-q_{\mathrm{L}}} + \lim_{q_{\mathrm{S}} \to 2} (1-q_{\mathrm{S}}) \left(\frac{(D_0/D_k)^{q_{\mathrm{S}}-2} \ln(D_0/D_k)}{-1} \right) \right) \right] D_0, \tag{B6}$$

$$= \left[\frac{1-q_{\mathrm{L}}}{2-q_{\mathrm{L}}} + \ln(D_k/D_0) \right] D_0, \qquad D_0 < D_k. \tag{B7}$$

REFERENCES

Bailey, M. E. 1976, Nature, 259, 290
Bernstein, G. M., Trilling, D. E., Allen, R. L., Brown, M. E., Holman, M., & Malhotra, R. 2004, AJ, 128, 1364
Bickerton, S. J., Kavelaars, J. J., & Welch, D. L. 2008, AJ, 135, 1039
Bracewell, R. 1986, The Fourier Transform and its Applications, 2nd edn. (New York: McGraw-Hill)
Brown, M. J. I. & Webster, R. L. 1997, MNRAS, 289, 783
Chang, H., King, S., Liang, J., Wu, P., Lin, L., & Chiu, J. 2006, Nature, 442, 850
Cooray, A. 2003, ApJ, 589, L97
Cooray, A. & Farmer, A. J. 2003, ApJ, 587, L125
Cox, A. N., ed. 2000, Allen's Astrophysical Quantities, 4th edn. (New York: AIP Press; Springer)
Dravins, D., Lindegren, L., Mezey, E., & Young, A. T. 1997, PASP, 109, 173
Dyson, F. J. 1992, QJRAS, 33, 45
Fraser, W. C. & Kavelaars, J. J. 2009, AJ, 137, 72
Fuentes, C. I. & Holman, M. J. 2008, ArXiv e-prints, 804
Gaudi, B. S. 2004, ApJ, 610, 1199
Gladman, B., Kavelaars, J. J., Petit, J.-M., Morbidelli, A., Holman, M. J., & Loredo, T. 2001, AJ, 122, 1051
Jones, T. A., Levine, A. M., Morgan, E. H., & Rappaport, S. 2006, The Astronomer's Telegram, 949, 1
Kenyon, S. J. & Bromley, B. C. 2004, AJ, 128, 1916
Liang, C.-L., Rice, J. A., de Pater, I., et al. 2002, astro-ph/0209509
McLean, I. S. 1997, Electronic imaging in astronomy. Detectors and instrumentation

Nihei, T. C., Lehner, M. J., Bianco, F. B., King, S.-K., Giammarco, J. M., & Alcock, C. 2007, AJ, 134, 1596
Pan, M. & Sari, R. 2005, Icarus, 173, 342
Press, W. H., Teukolsky, S. A., Vetterling, W. T., & Flannery, B. P. 1992, Numerical recipes in C. The art of scientific computing (Cambridge: University Press, —c1992, 2nd ed.)
Roques, F., Doressoundiram, A., Dhillon, V., Marsh, T., Bickerton, S., Kavelaars, J. J., Moncuquet, M., Auvergne, M., Belskaya, I., Chevreton, M., Colas, F., Fernandez, A., Fitzsimmons, A., Lecacheux, J., Mousis, O., Pau, S., Peixinho, N., & Tozzi, G. P. 2006, AJ, 132, 819
Roques, F., Doressoundiram, A., Dhillon, V., Marsh, T., Kavellars, J., Bickerton, S., Peixinho, N., Fitzsimmons, A., Colas, F., Lecacheux, J., Pau, S., Belskaya, I., & Mousis, O. 2004, AAS/Division for Planetary Sciences Meeting Abstracts, 36, # 03.09
Roques, F. & Moncuquet, M. 2000, Icarus, 147, 530
Roques, F., Moncuquet, M., & Sicardy, B. 1987, AJ, 93, 1549
Zhang, Z.-W., Bianco, F. B., Lehner, M. J., Coehlo, N. K., Wang, J.-H., Mondal, S., Alcock, C., Axelrod, T., Byun, Y.-I., Chen, W. P., Cook, K. H., Dave, R., de Pater, I., Porrata, R., Kim, D.-W., King, S.-K., Lee, T., Lin, H.-C., Lissauer, J. J., Marshall, S. L., Protopapas, P., Rice, J. A., Schwamb, M. E., Wang, S.-Y., & Wen, C.-Y. 2008, ApJ, 685, L157